



ELSEVIER



<https://doi.org/10.1016/j.ultrasmedbio.2022.01.010>

● Original Contribution

NUMERICAL STUDY OF ACOUSTIC HOLOGRAMS FOR DEEP-BRAIN TARGETING THROUGH THE TEMPORAL BONE WINDOW

DIANA ANDRÉS, NOÉ JIMÉNEZ, JOSÉ M. BENLLOCH, and FRANCISCO CAMARENA

Instituto de Instrumentación para Imagen Molecular (i3M), Universitat Politècnica de València, Consejo Superior de Investigaciones Científicas (CSIC), València, Spain

(Received 24 September 2021; revised 14 January 2022; in final form 16 January 2022)

Abstract—Acoustic holograms can encode complex wavefronts to compensate the aberrations of a therapeutical ultrasound beam propagating through heterogeneous tissues such as the skull, and simultaneously, they can generate diffraction-limited acoustic images, that is, arbitrary shaped focal spots. In this work, we numerically study the performance of acoustic holograms focusing at the thalamic nuclei when the source is located at the temporal bone window. The temporal window is the thinnest area of the lateral skull and it is mainly hairless, so it is a desirable area through which to transmit ultrasonic waves to the deep brain. However, in targeting from this area the bilateral thalamic nuclei are not aligned with the elongated focal spots of conventional focused transducers, and in addition, skull aberrations can distort the focal spot. We found that by using patient-specific holographic lenses coupled to a single-element 650-kHz-frequency 65-mm-aperture source, the focal spot can be sharply adapted to the thalamic nuclei in a bilateral way while skull aberrations are mitigated. Furthermore, the performance of these holograms was studied under misalignment errors between the source and the skull, concluding that for misalignments up to 5°, acoustic images are correctly restored. This work paves the way to designing clinical applications of transcranial ultrasound such as blood–brain barrier opening for drug delivery or deep-brain neuromodulation using this low-cost and personalized technology, presenting desirable aspects for long-term treatments because the patient’s head does not need to be shaved completely and skull heating is low. (E-mail: nojigon@upv.es) © 2022 World Federation for Ultrasound in Medicine & Biology. All rights reserved.

Key Words: Acoustic holograms, Therapeutic ultrasound, Neuromodulation, Blood–brain barrier opening.

INTRODUCTION

Transcranial focused ultrasound is an emerging technique with great potential for treating brain diseases in a non-invasive, non-ionizing manner. Ultrasound waves can penetrate skull bones and produce thermal and mechanical effects in the brain tissue (Carstensen 1976). These kinds of interactions constitute the basis of several treatments developed in recent years, ranging from thermal ablation, in which ultrasound absorption results in a localized temperature increase causing cell necrosis (Coluccia et al. 2014), to hyperthermia, in which ultrasound induces a mild temperature increase to enhance chemotherapy or radiation therapy (Tillander et al. 2016). In addition, with the use of high-amplitude and short pulses, ultrasound histotripsy can enable cavitation of bubble clouds to generate sharp lesions at the

targeted region through mechanical effects (Sukovich et al. 2018). At lower intensities, it also has been widely proven that focused ultrasound can disrupt the blood–brain barrier in a localized, safe and reversible manner (Konofagou et al. 2012; McDannold et al. 2012), enabling localized drug-delivery applications in the central nervous system. In addition, at lower acoustic intensities, the mechanical interaction of the waves can produce neuromodulation effects in different parts of the brain (Legon et al. 2020).

However, the presence of skull bones between the ultrasonic source and the target region of the brain is a major obstacle to the application of focused ultrasound in the brain. This wall of high stiffness and density protects the brain from mechanical loads, including mechanical waves such as ultrasound. Its high acoustic impedance and complex poroelastic and layered internal structure have strong scattering, refraction and attenuation effects on the propagating acoustic waves. This results in beam aberrations and poor focusing. Several

Address correspondence to: Noé Jiménez, Instituto de Instrumentación para Imagen Molecular (i3M), Camino de Vera S/N, València 46022, Spain. E-mail: nojigon@upv.es

systems have been proposed to overcome these drawbacks and take control of the acoustic focus, its location, size and shape. By use of a minimally invasive approach, intracranial ultrasound implants can be placed inside the skull to directly sonicate brain tissues, avoiding phase aberrations (Horodyckid *et al.* 2017). This technique requires craniotomy and, therefore, is suitable after surgical resection of a tumor, that is, a glioblastoma, to open the blood–brain barrier for delivery of post-operative chemotherapeutic agents. Fully non-invasive techniques are desirable, such as magnetic resonance (MR)–guided phased-array systems, which control the delay and amplitude of the vibration of each individual piezoelectric transducer to electronically steer to the focal spot and mitigate the aberrations produced by the skull (Lipsman *et al.* 2018). However, as these therapeutic sources require a wide aperture and the number of active transducers of state-of-the-art phased arrays is on the order of 1024/2048 elements, this approach results in large piezoelectric elements. In this way, the focal steering capabilities are limited by the emergence of diffraction grating lobes because active elements are separated more than half a wavelength. This novel technology stands out for its complexity and high cost, which makes it unattainable for many health and research centers. One approach to avoid magnetic resonance imaging (MRI)–guided systems is to use stereoscopic image guided single-element transducers, and use simulations to select the optimal transducer location to minimize beam aberrations (Pouliopoulos *et al.* 2020). Recent approaches include conformal helmet scaffolds, composed of a patient-specific 3-D–printed helmet designed to hold reusable phased-array transducer modules. These systems enable a near-normal incidence of multiple phased array modules, where the position of each transducer is determined by the location of the therapeutic target (Adams *et al.* 2021).

Recently, in response to the need for low-cost and non-invasive ultrasonic focusing systems, 3-D–printed acoustic lenses (Maimbourg *et al.* 2018) and acoustic holograms (Jiménez-Gambín *et al.* 2019) have been proposed. On the one hand, through the use of refractive 3-D–printed lenses, aberrations introduced by the skull can be compensated recovering the single focal spot of a focused transducer. When focusing in a single spot, the focal point reconstructed by a 3-D–printed lens can even be steered by mechanically moving the source (Maimbourg *et al.* 2019). On the other hand, acoustic holograms can perform better, reconstructing sharp acoustic images inside the brain using local resonances, such as Fabry–Perot longitudinal modes in a 3-D–printed elastic plate (Jiménez-Gambín *et al.* 2019). Acoustic holograms, first proposed for homogeneous media (Melde *et al.* 2016), can generate focal spots

whose shape and size can be controlled and modified to target a specific structure in the central nervous system. Recently, this technique has been tested *ex vivo* using human skulls (Jiménez-Gambín *et al.* 2020b) and validated *in vivo* for blood–brain barrier opening in mice (Jiménez-Gambín *et al.* 2020a).

Skull heating is a main concern when performing transcranial ultrasonic therapy, and it has been observed to be critical at thicker parts of the human skull, particularly at high ultrasound frequencies >1 MHz (Sun and Hynynen 1998; Connor and Hynynen 2004). When single-element transducers are used to tackle deep-brain nuclei, the elongated focal spot must be aligned with the therapeutic target, and a normal incidence is required to minimize beam refraction. This usually results in better targeting through the occipital and parietal bones (Qiu *et al.* 2020). However, the bone at the temporal window is thinner and more uniform. In fact, this location is usually selected for brain imaging (Aaslid *et al.* 1982). The thinness of this layer produces fewer aberrations and lower skull heating; therefore, it is desirable for transcranial ultrasound therapy. In addition, only a small amount of hair needs to be shaved, which can be a common concern for patients, particularly during long-term treatments. One deep-brain target of main interest is the thalamus, a bilateral structure involved in many processes such as consciousness, sleep cycle, integration of sensory data and supporting motor and language systems (Jones 2012). Recent studies performed thalamic neuromodulation in humans using single-element transducers (Schafer *et al.* 2020) revealing evidence of inhibiting effects (Legon *et al.* 2018). Evidence of recovery from coma in a patient by direct neuromodulation of these deep brain nuclei has been reported (Monti *et al.* 2016). However, when the thalamic nuclei are targeted through the temporal window using a single-element focused transducer, the therapeutic target is not completely aligned with the elongated focal spot of the ultrasound source.

In the work described here, we numerically studied acoustic holograms to target the thalamic nuclei in humans through the temporal window. By use of acoustic holograms coupled to a flat transducer, as illustrated in Figure 1, the skull aberrations can be compensated, and simultaneously, the shape of the focal spot and its location can be adapted to bilaterally target the thalamic nuclei. Five different strategies to design the holograms are presented, and their performance is compared with that of a reference focused transducer. As we will describe, holograms allow use of the temporal window to accurately focus acoustic energy at the thalamic nuclei. In addition, note that although control of the physical location of the system can be performed using mechanical or optical methods (Wu *et al.* 2018), these systems introduce some degree of uncertainty in the

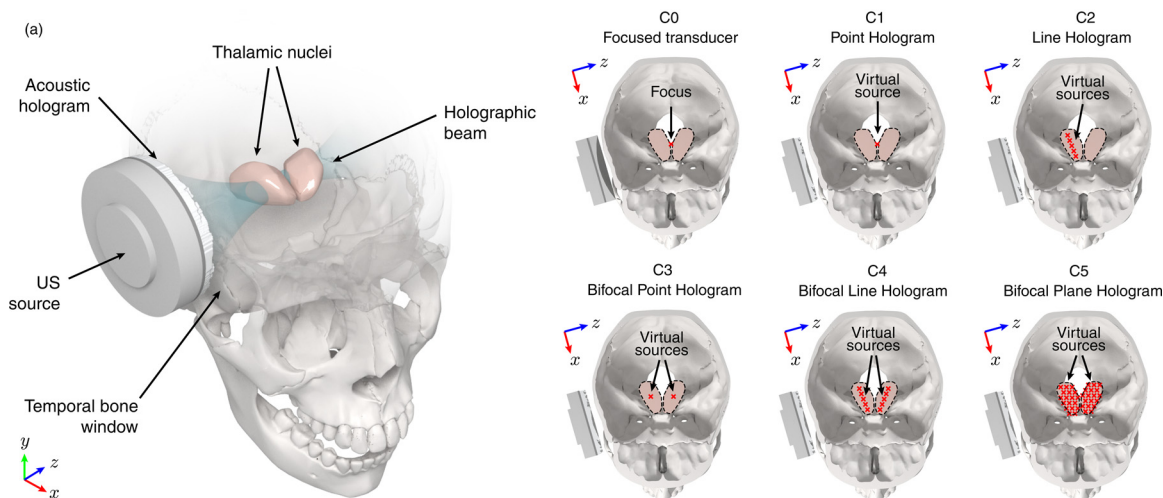


Fig. 1. (a) Scheme of the proposed device. An acoustic hologram is coupled to a flat circular ultrasound (US) source and located at the temporal bone window, targeting the deep-brain nuclei. Several configurations are studied: a reference focused transducer (configuration C0), a point hologram targeting the central point of the thalamic nuclei (C1), a line hologram targeting the center of the targets (C2), a bifocal point hologram targeting each nucleus (C3), a bifocal line hologram targeting each nucleus (C4) and a bifocal plane hologram targeting each nucleus (C5).

positioning. Therefore, we studied aberrations introduced by misplacement of the source and evaluated the robustness of the resulting field against misalignments. We have studied how the use of acoustic holograms through the temporal bone window results in a lower temperature increase as compared with that for other thicker skull bones, such as the parietal or frontal bones. Finally, the performance of holograms on different participants using the same lens for different patients and patient-specific lenses was studied.

METHODS

We use a flat circular transducer with an aperture of $2a = 65$ mm. It is located at the temporal bone window, at a distance of 15 mm from the skin to allow for inclusion of a holographic lens (Fig. 1). A second transducer with characteristics similar to those used for thalamic focusing through the temporal bone window (Monti et al. 2016) is employed. It is a spherically focused transducer with a radius of curvature of $F = 80$ mm and same aperture as the first (f -number = 1.23), also located at the temporal bone window at a distance of 13 mm from the skin. The focused transducer is aligned to focus at the center between both thalamic nuclei, in the middle of the thalamus, as represented in Figure 1, configuration C0. Both sources are excited with a 650-kHz sinusoidal signal.

To design the hologram we used a time-reversal simulation method, according to the procedure described by Jiménez-Gambín et al. (2019). The tomographic image of the skull used in this study was acquired with a GE

LightSpeed VCT 64 scanner (GE Medical Systems, Milwaukee, WI, USA) from an anonymous patient using a resolution of 0.488 mm and slice resolution of 0.625 mm. To introduce the skull in the numerical simulations and match the numerical grid, it has been interpolated with an isotropic resolution of 0.39 mm, which corresponds to $\lambda/6$ at the transducer frequency. The computerized tomography (CT) linear X-ray attenuation data, in Hounsfield units, are converted to density and sound speed maps using empirical linear relationships (Schneider et al. 1996; Mast 2000). Values of mean and maximum sound speed and density at the skull are as follows: $c_{\text{mean}} = 2332.6$ m/s, $c_{\text{max}} = 3100$ m/s, $\rho_{\text{mean}} = 1611.3$ kg/m³, $\rho_{\text{max}} = 2190$ kg/m³. Acoustic attenuation of the skull has been set constant, as it has been proved that a variation in this value along the skull weakly affects acoustic transmission (Robertson et al. 2017), and its value was set to 8.371 dB/(cm-MHz ^{γ}), according to Cobbold (2006), using $\gamma = 1.1$. Brain tissue has also been considered in the studies; it is defined as the whole interior volume of the skull, with density, speed of sound and acoustic absorption of 1000 kg/m³, 1560 m/s and 0.659 dB/(cm-MHz ^{γ}), respectively. Both the skull and the transducer are surrounded by water, with a density of 1000 kg/m³, sound speed of 1522 m/s and absorption of 0.0009 dB/(cm-MHz²).

The selected therapeutic target of this study is the thalamus. The location and shape of this structure have been extracted from the human atlas published online and available open-access as the International Consortium for Brain Mapping (ICBM) template from the Laboratory of Neuro Imaging (Yushkevich et al. 2006). The volume and shape of the brain have been extracted from

the same MR image. As the segmented MRI data do not correspond to the skull in the CT image, rotations and linear homothetic transformations were performed until the brain extracted from the MR image fit into the cranial cavity, to ensure the correct location of the thalamus inside the skull model. The volume of both thalami is 7.9 cm^3 , and the volume of the brain is 1523 cm^3 .

Numerical simulations were performed using a pseudo-spectral time-domain method in the k -space, implemented in the open-source k-Wave software (Treeby and Cox 2010). In the case of the reference focused transducer (configuration C0 in Fig. 1), the acoustic field is obtained directly by propagating the converging wavefront generated by the source. In the case of the holograms, several configurations are studied: a point hologram targeting the central point of the thalamic nuclei (configuration C1), a line hologram targeting the center of the targets (configuration C2), a bifocal point hologram targeting each nucleus (configuration C3), a bifocal line hologram targeting each nucleus (configuration C4) and a bifocal plane hologram targeting each nucleus (configuration C5), as illustrated in Figure 1. To design the holograms, a time-reversal procedure is performed. First, a set of virtual acoustic monopole sources are located at the target, each set according to the corresponding configuration. Then, in a first simulation, the resulting field radiated by the virtual sources is recorded at a holographic surface in the x - y plane, $P_H(x,y)$, located at distance $z = d$ from the source (Fig. 2). The temporal inversion is performed by complex-conjugating the recorded pressure field at the holographic plane, resulting in a field $P_H^*(x,y)$.

Then, the holographic surface is divided into squared pixels of $0.39 \times 0.39 \text{ mm}^2$, equal to the resolution of the simulation grid, each pixel corresponding to a pixel of the holographic lens (Fig. 2). Each pixel of the lens represents a different height, given by the function $h(x,y)$. We assume they vibrate longitudinally like an elastic Fabry–Perot resonator, whose complex transmission coefficient at the holographic plane is given by

$$T = \frac{2Z_n e^{ik_0(d-h)}}{2Z_n \cos(k_L h) + i(Z_n^2 + 1) \sin(k_L h)} \quad (1)$$

where d is the distance from the bottom of the lens to the holographic surface, $Z_n = Z_L/Z_0$ is the normalized impedance, $Z_0 = \rho_0 c_0$, $k_0 = \omega/c_0$, ρ_0 and $Z_L = \rho_L c_L$, $k_L = \omega/c_L$, c_L , and ρ_L , are the acoustic impedance, wavenumber, sound speed and density in water and in the lens material, respectively. At each point in the surface, that is, for each pixel of the lens, we use an interpolation method to find the minimum height function $h(x,y)$ in eqn (1) that fulfills $\arg[P_H^*(x,y)] = \arg[T(x,y)]$. Once the height function is found, holograms can be constructed,

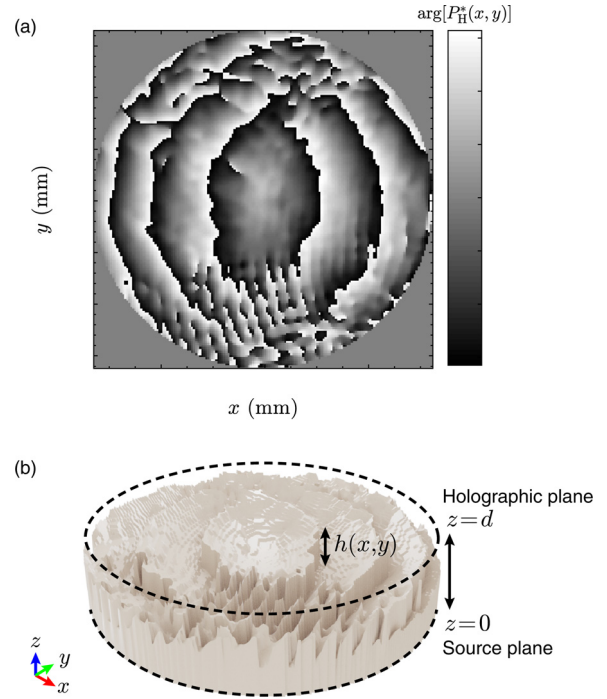


Fig. 2. (a) Phase of the field after phase conjugation recorded at the holographic surface for the single-line hologram configuration. (b) Rendering of the corresponding hologram revealing the holographic plane at $z = d$. The flat circular source is located at the bottom of the lens.

resulting in surfaces with a total of 22,129 pixels and a maximum height of 10.8 mm. Note that each of them acts as a phased-array emitter, allowing accurate control of the phase profile. In this way, the compensation of the aberrant effects of the skull and the time-reversal focusing toward the positions of the original virtual sources are simultaneously encoded on the high-density pixel hologram. Three-dimensional models of the lenses for each configuration are provided in the Supplementary Data (online only).

Finally, a simulation was carried out to retrieve the acoustic field produced by the holograms. All designed lenses use the material properties corresponding to Clear resin (Formlabs, Somerville, MA, USA), a photopolymer used for 3-D printing. The speed of sound and acoustic absorption of this material have been experimentally measured with pulse-echo techniques in cylindrical samples of different height, while the density has been calculated with knowledge of the dimensions of each cylinder and its mass. These experiments resulted in $\rho_L = 1170.8 \text{ kg/m}^3$, $c_L = 2580.1 \text{ m/s}$ and $\alpha_L = 2.871 \text{ dB/(cm-MHz)}$. These values match those reported for similar materials (Melde *et al.* 2016; Jiménez-Gambín *et al.* 2019, 2020b). In all simulations, the source was driven with a 100-cycle sinusoidal tone burst of 650-kHz frequency and 1-Pa amplitude at the surface of the source. Each simulation was running during $300 \mu\text{s}$ so the pulsed burst could cross

the medium twice. This time was considered for both backward and forward propagation simulations, so that multiple internal reflections of the acoustic wave in the skull could be encoded by the hologram.

To study the robustness of ultrasound holograms under small deviations between the acoustic lens and the skull, several parameters were studied under rotations and displacements of the lens: maximum pressure gain at the focus position, total focus volume, sonicated target volume and out-of-target sonicated volume. Normalized peak pressure is calculated as the pressure gain relative to the pressure at the transducer surface and to half the average pressure at the exit of the holographic lens for the focused transducer and holograms, respectively. Volumes are calculated as the region with a pressure gain between the maximum and -3 dB for each focus separately. Performance under rotations of 1.25° from 0° to 17.5° and under translations of 1 mm from 1 to 8 mm in the y -axis have been studied for the focused transducer and C2, C3 and C4 configurations.

The skull heating rate was used as a figure of merit to quantify the capacity of the acoustic beam to raise the temperature of the skull. We first calculated the acoustic pressure field at steady state. The particle velocity vector, assuming a harmonic wave, is calculated as $v_i = 1/(i\omega\rho)\partial p/\partial x_i$, with $i = x, y, z$, and period-averaged acoustic intensity is calculated as $I = \text{Re}(p\mathbf{v}^*)/2$, where $(\bullet)^*$ denotes complex conjugation. Then, the total heating rate in a given volume is

$$W_Q = \int_V Q \cdot dV \quad (2)$$

where $Q = 2\alpha I$ is the heating rate per unit volume, α being the medium attenuation value and I the magnitude of the acoustic intensity.

Finally, additional simulations were carried out on different participants to study the performance of the same lens on different patients. The simulation study for the C1 configuration was repeated for three different anonymous patients (participants 2–4), targeting the same region from the right temporal bone. For each additional participant, two calculations were performed. First, a lens was created *ad hoc* for each patient. Note that the target segmentation for participant 1 was used for participants 2–4, but we considered the new skull anatomy, inner structure and acoustical properties. Second, the lens created for participant 1 was used for participants 2–4.

RESULTS

Focused ultrasound transducer

The results for the reference focused transducer are summarized in Figure 3. This source was first simulated

in a homogeneous medium (water) and, then, including the human head. Figure 3a is a 3-D rendering, obtained by using a maximum intensity projection method, of the magnitude of the acoustic field for the transcranial propagation through the temporal bone window. That the focused beam presents strong aberrations can be visually identified. A detailed image is provided in the sagittal and coronal sections in Figure 3 (b and c, respectively). Note that the transducer was located carefully to grant normal incidence and the cartesian axis are aligned to the transducer axis, so the images do not exactly correspond to anatomical sagittal and coronal sections. While the energy roughly focuses around the geometrical focus of the transducer, which has been located in the center of the thalamus (configuration C0), the ultrasound beam covers several areas outside the target (Fig. 3c). In fact, the maximum sound pressure inside the brain does not correspond to the maximum in the main focal spot, but to a secondary lobe. A large amount of energy is focused at the prefocal zone, outside the target. A total of 0.28 cm^3 of both thalami was sonicated at a pressure higher than -3 dB below the peak pressure level, which represents 3.6% of the total thalamic volume, while 1.208 cm^3 was sonicated outside the therapeutic target, which is a 0.08% of the total brain volume, including the thalamus.

Figure 3 (d–f) illustrates the normalized cross-section of the maximum pressure field in the z -, y - and x -directions for the focused transducer considering the human tissues and the corresponding field in water. It can be observed that the elongated focal spot does not accurately fit the target, represented by *dashed lines*. The maximum focal pressure gain in water for this transducer is $17.8 p/p_0$, whereas when considering that in the skull and the brain is $4.7 p/p_0$, where p_0 is the pressure at the transducer surface, the skull and brain tissues introduce a loss in pressure gain of 5.8 dB according to these results. In the axial direction (Fig. 3d), the depth-of-field of the focused transducer including the skull (36.5 mm) is longer than that of the right half of the thalamus (13.2 mm), and therefore, acoustic energy is also focused at the third ventricle in the midline between the two halves of the thalamus. In the lateral direction, the full width at half-maximum of the beam (4.25 mm in the y -direction and 8.1 mm in the x -direction) is narrower than that of the target (16.8 and 26.2 mm, respectively). Aberrations introduced by the skull become more evident in Figure 3f, where multiple lateral lobes appear. The defocusing effect produced by the skull usually increases the sonicated volume inside the target (1.48 cm^3 in this simulation compared with 0.43 cm^3 obtained with the focused source in water), which could be considered positive. However, it is an uncontrollable phenomenon that also

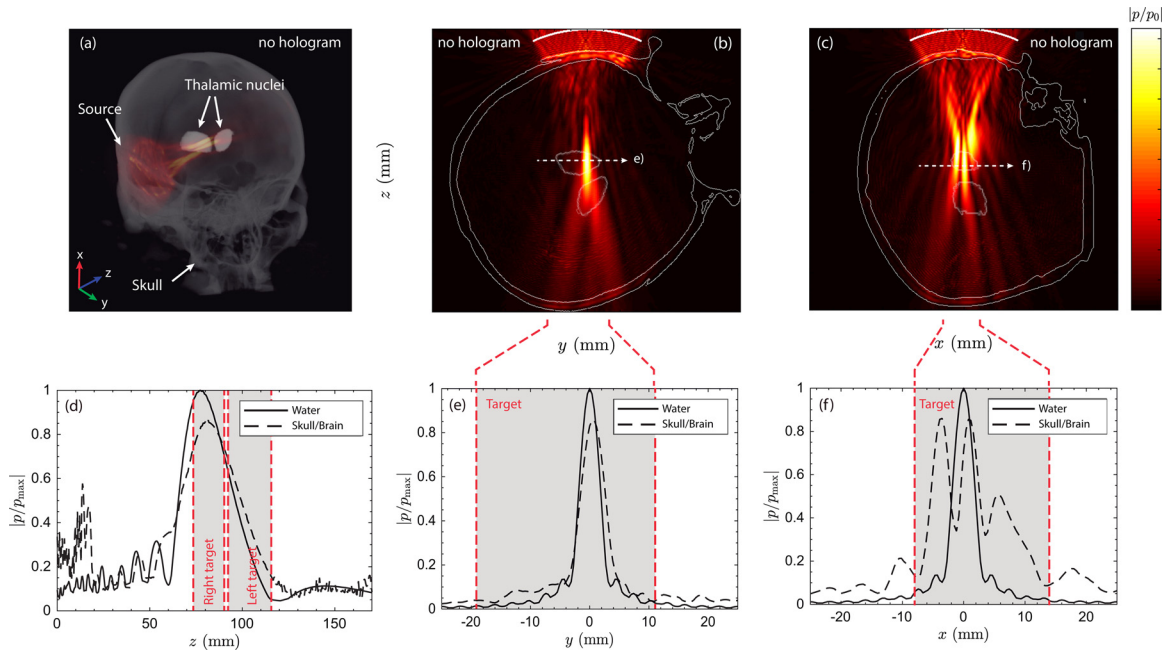


Fig. 3. (a) Three-dimensional view of the studied configuration using the focused source (C0). Maximum intensity projection of the computerized tomography (CT) data (*gray colormap*), segmented thalamic nuclei (*white areas*) and maximum intensity projection of the acoustic field (*red colormap*). (b, c) Cross-section of the acoustic field in (b) the y - z plane (quasi-coronal cut) and (c) the x - z plane (quasi-sagittal cut); colormaps are normalized to p_0 . (d-f) Normalized peak pressure in water and through the skull along the (d) z -axis, (e) x -axis and (f) y -axis.

increases the sonication in out-of-target regions (1.19 cm^3 in this simulation).

Holograms for skull aberration correction

With the aim of correcting skull defocusing, a single virtual source was set in the center of both thalami, located at $(0, 0, 101)$ mm in cartesian coordinates, corresponding to configuration C1 in Figure 1. The acoustic field produced by this hologram is illustrated in Figure 4 (b, d). It can be seen that the focal zone is similar to that of the focused transducer including the skull (Fig. 4f), but lateral lobes caused by defocusing and aberrations are not present. The lens corrects beam aberrations, producing an ultrasonic field equivalent to that of a focused source in a homogeneous medium. The acoustic image of a single virtual source (C1) is a diffraction-limited focal spot, whose full width at half-maximum is 5.2 mm, as compared with 3.9 mm for the focused source in water. In this way, while this configuration corrects aberrations, the width of the beam is still narrower than the selected therapeutic target.

To laterally magnify the focus in one dimension to cover a greater volume of the thalamic nuclei, 22 virtual sources were located in a line along the midline of the thalamic nuclei, in the x - y plane (configuration C2 in Fig. 1). A 3-D rendering of this configuration and the resulting field is provided in Figure 4a. The resulting

field produced by the C2 hologram is illustrated in Fig. 4 (c, e) in the z - y and x - y planes, respectively. By use of this hologram, the focal spot widens in the lateral dimension while the aberrations introduced by the skull are still compensated.

Both holograms are compared with the acoustic field of the focused transducer in Figure 4 (g-i). In the axial direction, the elongated focal spot of holograms C1 and C2 is 41.7 and 52 mm, respectively, as compared with 37 mm for the focused source. As illustrated in Figure 4g, the axial field does not accurately match the target region. However, note that neither C1 nor C2 was designed to control the beam in the z -direction. In the transverse directions (Fig. 4h, 4i) secondary lobes of the focused transducer are controlled in both transverse directions, y and x . In the y -direction, the C2 hologram widens the beamwidth to 7.8 mm (50% larger than the single-virtual-source hologram, see Fig. 4i). However, as virtual sources were arranged over a line only in the y -direction, the beam is not enlarged in the x -direction (see Fig. 4i).

For the single-virtual-source hologram, the amplitude of the pressure at the focal spot is $7.6 p/p_0$, where p_0 is defined as half the average pressure at the exit plane of the holographic lens for all the holograms studied. We use this reference because at the exit of the lens, the total pressure is the superposition of radiated waves and reflected waves by the skull (see Fig. 4b). The increase

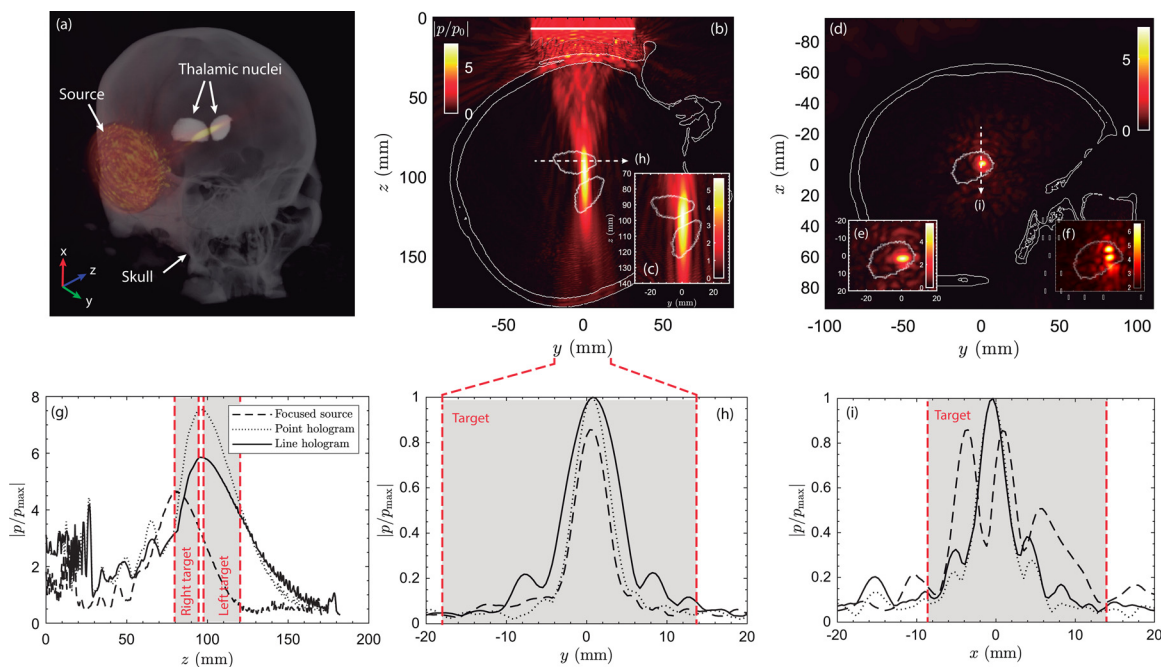


Fig. 4. (a) Three-dimensional scheme of the line hologram acoustic field. (b, c) Coronal cuts of the (b) point hologram (C1 configuration) and (c) line hologram (C2 configuration). (d–f) Axial cuts for the (d) left thalamus of the point hologram, (e) left thalamus of the line hologram and (f) focused transducer. (g) Lineal cut along the z -axis at the maximum pressure point for the focused transducer, point hologram and lineal hologram. (h) Normalized pressure comparison in a cut along the y -axis. (i) Normalized pressure comparison in a cut along the x -axis.

in amplitude, compared with the focused source case ($p/p_0 = 4.7$), is due to the correction of the aberrations, which results in sharper focusing.

In addition, by the use of multiple virtual sources as in configuration C2, maximum pressure at the focus is increased to $5.9 p/p_0$. Note that this configuration produces a defocused beam of controlled width without aberrations. As compared with the focused transducer including the skull, the increase in pressure amplitude at the focal spot is 2.1 and 0.9 dB for configurations C1 and C2, respectively. Point (C1) and line (C2) holograms sonicate 5.2% (0.41 cm^3) and 8.5% (0.68 cm^3) of the total thalamic volume, respectively, compared with the 3.6% (0.28 cm^3) sonicated with the focused source, and the sonicated volume outside the target is 0.19 cm^3 (0.013%) and 0.77 cm^3 (0.05%), respectively, compared with 1.2 cm^3 (0.08%) with the focused source.

With use of the focused transducer, the ratio between sonicated thalamic and brain volumes is 0.23. With use of the C1 configuration it is 2.16, and with C2, it is 0.88. The thalamic-to-brain sonicated volume ratio is 9.4 and 3.8 times better when using point and line holograms, respectively.

Holograms for bifocal targeting

Although the previous acoustic holograms can mitigate the skull aberrations and increase the target

sonicated volume, further focusing improvements could be made to sonicate bilateral structures in the deep brain. Configurations using several sets of virtual sources distributed along the bilateral nuclei of the thalamus, as illustrated in Figure 1, are described in this section.

First, a pair of virtual sources have been located at each part of the thalamus, as illustrated in configuration C3 in Figure 1. As we are sonicating through the temporal bone window, both structures appear to be almost in the same line with respect to the transducer. To individually treat them and optimize the target–brain sonication ratio, both sources have been steered in the x -axis, as represented in Figure 5 (a–c). With this configuration, 4.5% of the target structure has been treated (0.36 cm^3), while only 0.45 cm^3 of the brain is affected, which represents a 0.03% of the brain volume. Pressure gains at the focal points arrive at $5.84 p/p_0$ and $3.7 p/p_0$ at the right and left thalami, respectively. The ratio between sonicated thalamic and brain volumes with this configuration is 0.79.

To further improve these results, a bifocal wide hologram has been created by locating virtual sources in two lines at different heights of the deep brain structures, which is represented in configuration C4. In this case we treat 1.36 cm^3 of both thalami (17.1%) in just one sonication. The sonicated volume outside the target is 4.94 cm^3 (0.32%), greater than in the other systems studied,

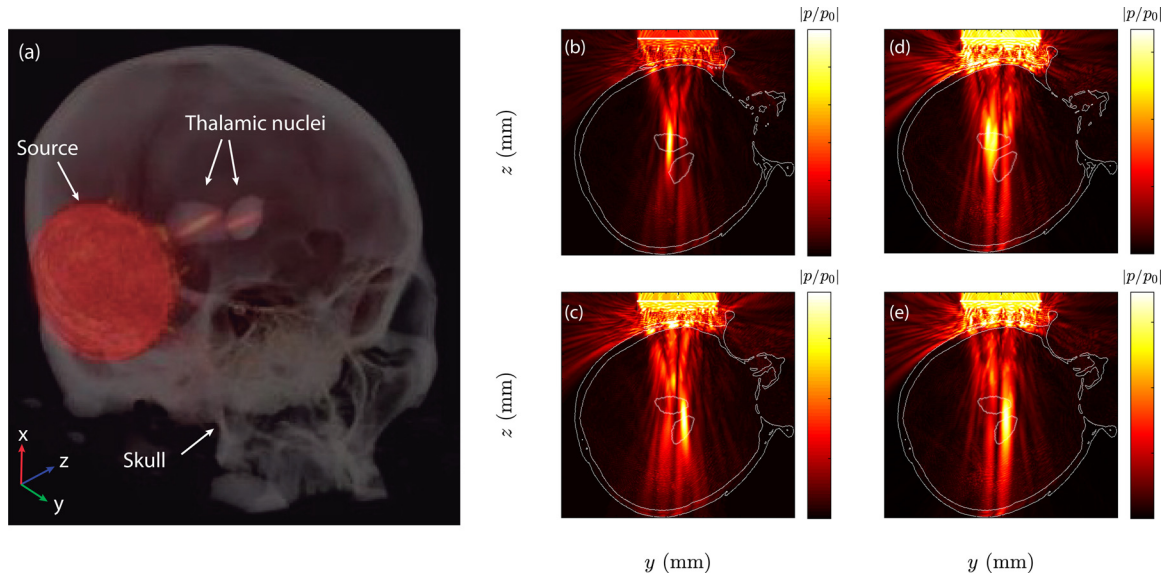


Fig. 5. (a) Three-dimensional representation of bifocal sonication with hologram. (b, c) Cuts for (b) left and (c) right thalamus point holograms. (d, e) Cuts for (d) left and (e) right thalamus plane holograms.

and the pressure gain is $3.9 p/p_0$ and $3.4 p/p_0$ at the right and left thalami, respectively. The thalamic-to-brain sonicated volume ratio with this configuration is 0.28.

A last hologram was made by locating two planes of virtual sources at the same x -position as in the two-point hologram and following configuration C5. The resulting acoustic field is illustrated in Figure 5 (d, e). We treat 1.21 cm^3 (15.3%) of the thalamus and we sonicate 5.84 cm^3 (0.38%) of the brain, with pressure gains of $3.4 p/p_0$ and $3.3 p/p_0$ at the left and right thalami, respectively. In this case, the ratio between sonicated thalamic and brain volumes is 0.21. The studied cases are compared in Table 1.

Robustness against misalignment

To evaluate the robustness of our proposal, we studied the accuracy of ultrasound holograms inside the brain when rotation and translation errors are made, as described in the Methods section. Figure 6 is an example

of the pressure field degradation under a progressive rotation for the line hologram (C2). The pressure scale is normalized to the maximum at 0° rotation. The focal quality parameters of the parametric study are illustrated in Figures 7 and 8. Figure 7 summarizes the focusing performance as a function of a rotational misalignment, while Figure 8 summarizes it as a function of a lateral linear translation.

For the focused transducer, its focus quality does not change under rotation from the center of the skull. The main change in sonicated volumes and peak pressures is due to the secondary lobes that appear because of the aberrations introduced by the skull. The maximum change in pressure values is 8% of the original pressure gain, and sonicated volumes of the brain and both thalami remain almost constant. As the angle of incidence of the focused sound waves is always normal to the skull, the skull-transducer relative location does not affect the focus shape. Similar results are obtained while the skull

Table 1. Thalamus and brain volumes sonicated in each case*

Configuration	Volume, cm^3 (%)		Volume ratio (a.u.)	Maximum pressure (p/p_0)
	Target	Out of target		
C0. Focused transducer	0.281 (3.6%)	1.208 (0.08%)	0.23	4.7
C1. Point hologram	0.413 (5.2%)	0.191 (0.013%)	2.16	7.6
C2. Line hologram	0.675 (8.5%)	0.767 (0.05%)	0.88	5.9
C3. Bifocal point hologram	0.356 (4.5%)	0.452 (0.03%)	0.79	5.8
C4. Bifocal line hologram	1.357 (17.1%)	4.937 (0.32%)	0.28	3.9
C5. Bifocal plane hologram	1.214 (15.3%)	5.839 (0.38%)	0.21	3.4

* Percentages are calculated with respect to total thalamus volume (target volume column) and total brain volume, including thalami (out-of-target volume column). The volume ratio is the ratio of target to out-of-target sonicated volumes.

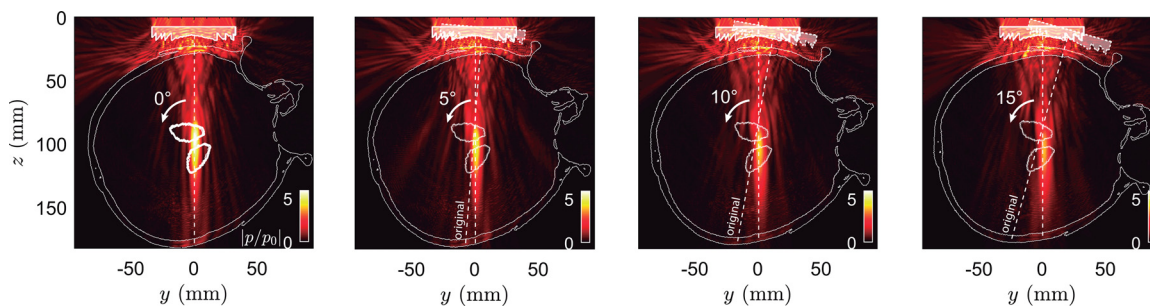


Fig. 6. Example of how a misalignment between the source and the target affects the focusing performance of the hologram. In this example (configuration C2), a rotation with respect to the central point of the thalamic nuclei is illustrated.

is horizontally translated from its original location, with a maximum change of pressure gain at the focus of 3% (see Figs. 7a and 8a).

For the line hologram, the maximum pressure decreases with the rotated angle and treated volumes increase, which means that the hologram loses resolution when it is not correctly positioned. At 17.5° of rotation, the acoustic pressure at the focus is reduced by 32% of the original value and the volume outside the target is 8.3 times greater. Also, the target volume covered is increased 1.5 times compared with the original location. For rotation angles below 5° , both volumes outside and inside the target remain almost constant ($<10\%$ of increase) while the difference in pressure gain is 15%. In terms of translation error, the same behavior in pressure values is observed for translation errors up to 6 mm (Figs. 7a and 8a).

In the case of the C3 configuration, the right focus, which is mainly laterally steered in the y -axis, exhibits a higher pressure amplitude and has a more delimited shape than the left focus, which was steered also in the x -axis. When rotating the lens 5° around the skull, the loss in pressure at the right focus is 21%, while for 17.5° , this loss is 48%. A similar loss of 24% is obtained with a translation misalignment of 5 mm, being 40% at 8 mm. If we study the left focus, for 5° we observe a pressure loss of 29%, while for 17.5° the amplitude reduction is 24%. A similar value is obtained with a translation misalignment of 6 mm (24%), whereas at 8 mm the loss is 22% (see Figs. 7a and 8a). Target volume sonicated by both foci with this configuration is 0.32 cm^3 at the original location, increasing to 0.36 cm^3 for a rotation of 5° . A similar value is observed for a translation error of 5 mm, and the volume is increased to 1.48 cm^3 when the rotation is 17.5° , which is almost five times greater than that in the original location. At the maximum translation error studied (8 mm), the target sonicated volume is three times greater. This is caused by the defocusing of the beam, which spreads the energy, covering a greater volume of

the thalamic nuclei. Nevertheless, sonicated brain volume outside the target follows the same tendency: at 5° the sonicated volume is increased by a factor of 3, the same as that at a translation error of 5 mm, and at 17.5° this increase is almost 30 times the volume covered while the transducer-lens system is located in the original position. For translation errors, at 8 mm, the brain sonicated volume is 13 times greater. These values indicate that large misalignments result in high defocusing, as expected, but for relatively small errors, for example, a rotation of 5° or a translation of 4 mm, the acoustic images are still generated with good quality. Note the wavelength at 650 kHz in water is 2.3 mm, so images are restored even for misalignments greater than the wavelength (see Figs. 7b–d and 8b–d).

The last hologram studied is that corresponding to the C5 configuration. This hologram exhibits behavior similar to that of the C3 configuration. Both foci had a similar pressure gain in the original location. When rotating 5° , the amplitude loss is 17% and 6% for the left and right focus, respectively (see Figs. 7a and 8a). For a 5-mm translation error, the loss is 18% and 13%, respectively. At higher rotation angles and translation distances, pressure values for the left focus remain constant; for a rotation of 17.5° and a translation of 8 mm, the pressure loss was about 18%. On the other hand, for the right focus, a decrease of 31% was reached for a rotation of 17.5° , and a loss of 44% was observed for a translation of 8 mm. Sonicated volumes in and outside the target are almost constant; the variations are 1.5 times the original value for rotations $<5^\circ$ and translations <4 mm. These sonicated volumes increase for greater rotation or translation errors. The sonicated target volume reaches a maximum, where a volume 2.4 times greater than the original was observed for a rotation of 10° . At this rotation, the sonicated brain tissue is 4.5 times larger than in the original position. At the maximum translation error studied (8 mm), the sonicated target volume is 2.5 times larger and the sonicated brain tissue is 5.3 times larger than in the original position (see Figs. 7b–d and 8b–d).

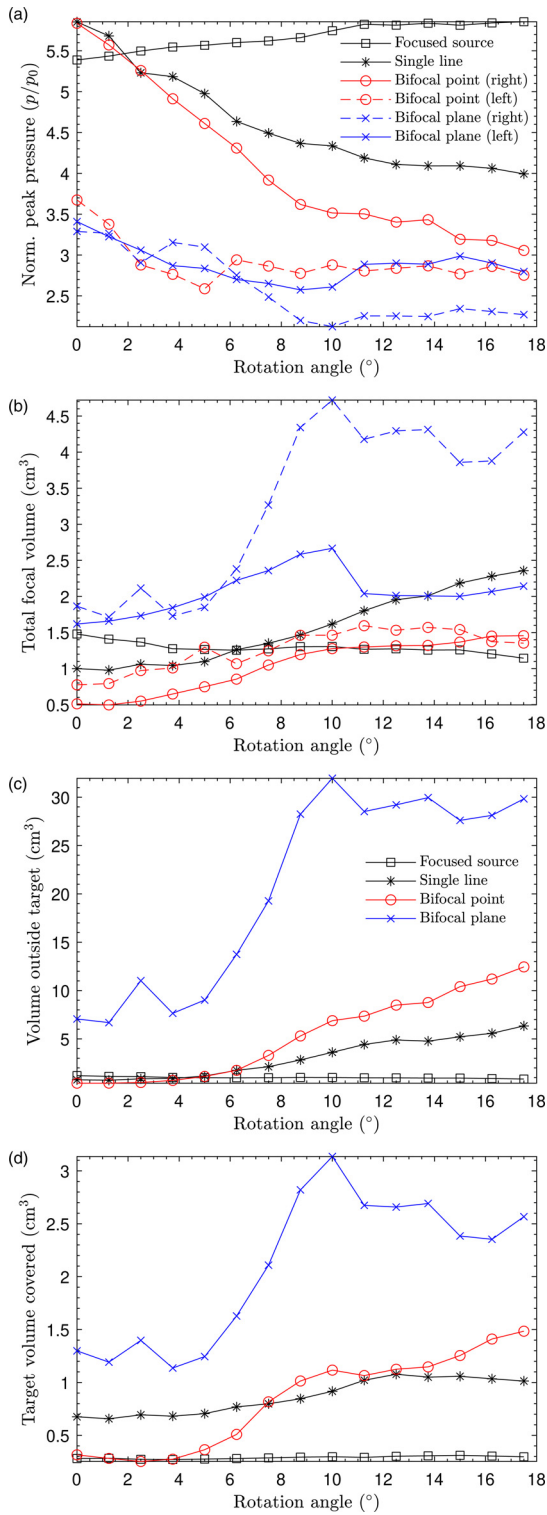


Fig. 7. Parametric study of focusing performance as a function of a rotational misalignment. (a) Maximum pressure at focus, normalized. (b) Focal volume. (c) Out-of-target volume. (d) In-target volume.

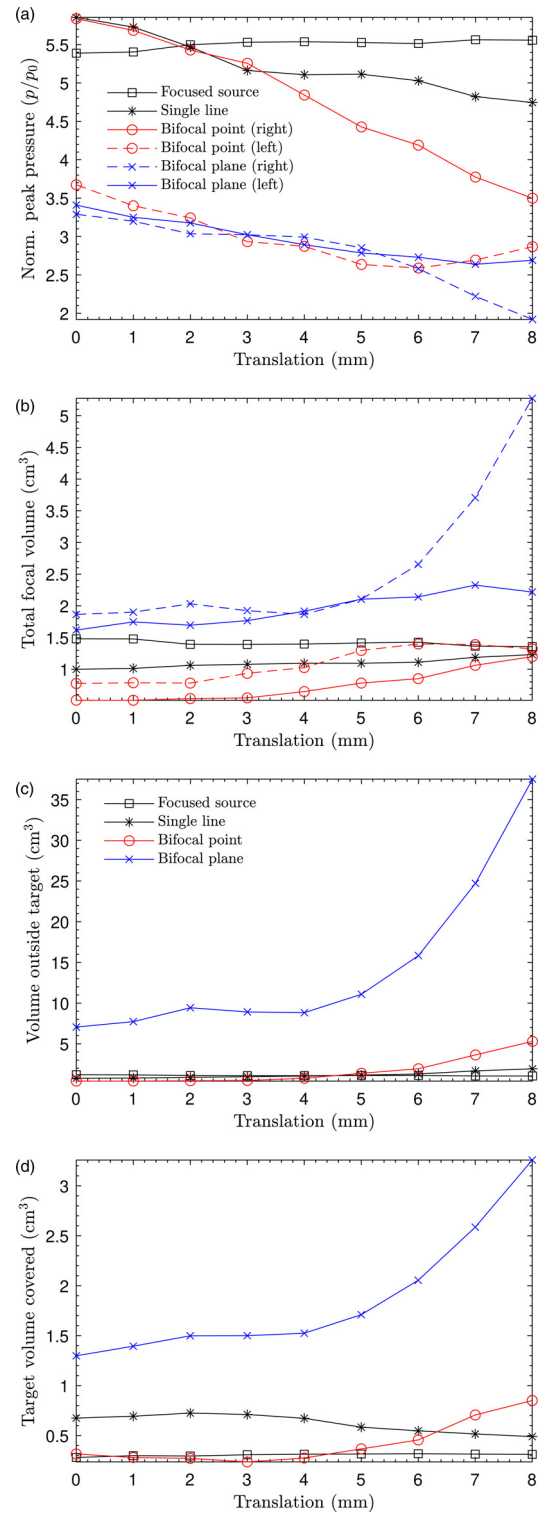


Fig. 8. Parametric study of focusing performance as a function of a lateral linear translation. (a) Maximum pressure at focus, normalized. (b) Focal volume. (c) Out-of-target volume. (d) In-target volume.

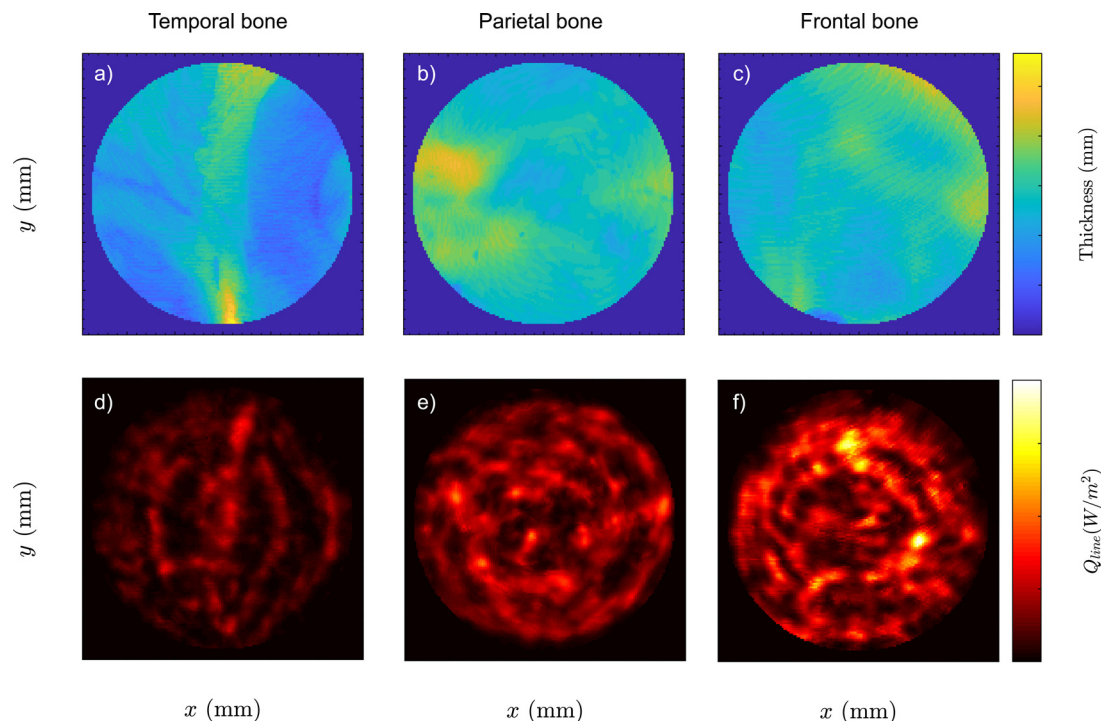


Fig. 9. Skull thickness measured at the (a) temporal bone window, (b) parietal bone and (c) frontal bone. (d–f) Heating rate per unit area obtained when targeting the holographic beam through the (d) temporal bone window, (e) parietal bone and (f) frontal bone.

Note that this behavior is similar for all holograms studied.

Skull heating rate

We studied the heating rate by targeting the thalamus through different regions of the same skull. We designed holograms to target the same location, that is, a point between both thalamic structures (C1 configuration). The transducer is located at the temporal bone window, the parietal bone and the frontal bone. Bone thickness at each area is illustrated in Figure 9 (a–c). The thickness is measured on a circle about 55 mm in diameter, matching the projection of the active hologram aperture on the bone surface. Average values of their thickness are 4.34, 5.98 and 5.69 mm for the temporal, parietal and frontal bones, respectively. The skull heating rate is calculated as described under Methods, considering that a peak pressure of 0.5 MPa is achieved at the target. The obtained total heating rate (W_D) was 0.39, 0.74 and 0.99 W for the temporal, parietal and frontal bones, respectively. The heating rate per unit area is illustrated in Figure 9 (d–f). Average heat capacity of the frontal bone and the parietal bone are 392 and 294 W/m^2 , respectively, while for the temporal bone it is 149 W/m^2 , which is less than half the heat capacity of the other two bones. As expected, thicker bones result in higher heating rates.

Patient-specific lenses

Finally, we describe the results of the study for different patients. The first set of simulations using the lens designed for participant 1 (C1 configuration) but focusing on participants 2–4 is illustrated in Figure 10 (a–c). It can be observed that the focal spot is not perfectly reconstructed, and strong aberrations distort the focal spot. The total gain for participants 2–4 is 2.0, 3.1 and 2.5, respectively. However, when a hologram is designed *ad hoc* for each patient, aberrations are corrected as illustrated in Figure 10 (d–f). By use of patient-specific lenses, the total gain for participants 2–4 rises to 4.4, 5.5 and 4.9, respectively. In addition, by use of a personalized lens, the side lobes are strongly reduced, and the strong secondary focal spots are no longer observed. These data indicate that the skull aberrations are patient specific even when targeting from the temporal bone window using a 50-mm aperture system.

DISCUSSION

Several strategies for designing ultrasound holograms using virtual sources to enhance sonicated thalamic tissue and correct skull aberrations are discussed in this work. While designed to target a point, holograms allow for aberration correction, and the resulting gain is increased as compared with that for the focused source,

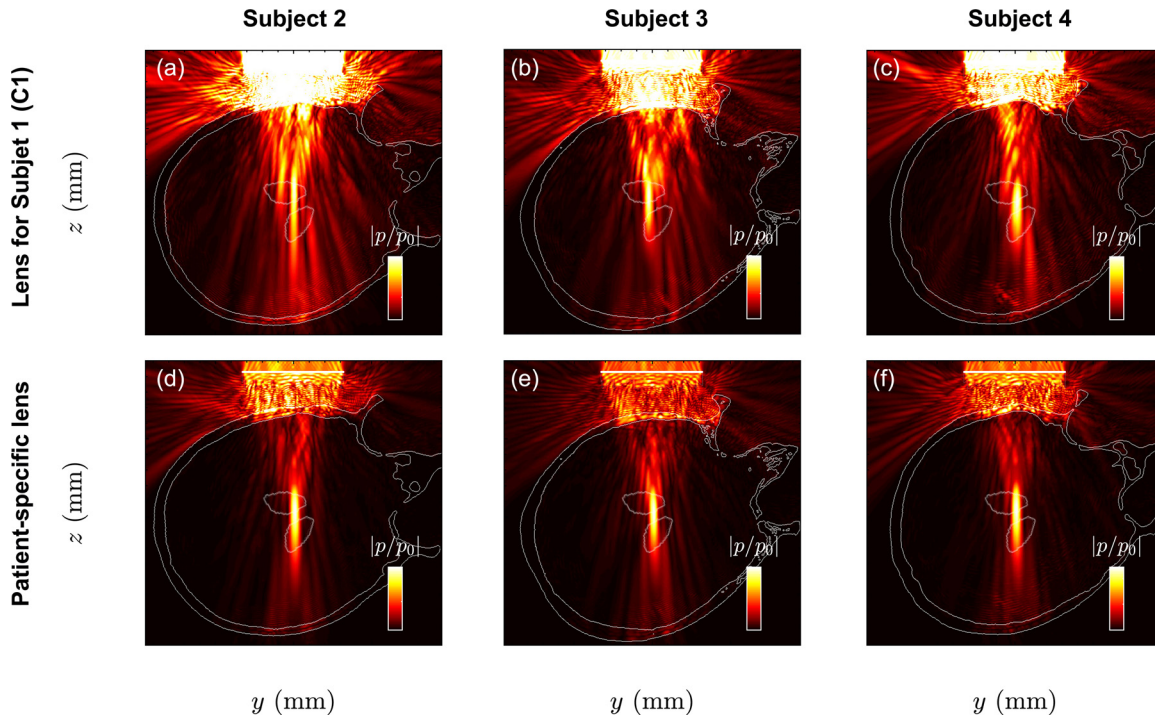


Fig. 10. (a–c) Acoustic field simulated using the hologram designed for participant 1 but focusing on participants 2–4. (d–f) Acoustic field simulated using a patient-specific hologram.

for example, 1.6 times higher. Simultaneously, when designed to target a unique focal point, holograms can minimize the out-of-target volume, 6.3 times less compared with the focused source, indicating the ability of these lenses to mitigate aberrations. On the other hand, holograms allow adaptation of the acoustic focus, that is, the acoustic image, to the shape of the therapeutic target, in this case the two bilateral nuclei of the thalamus. In this way, a much higher volume of the target can be covered by the therapeutic beam, which can be useful for medical applications that require good cover of the target. The greatest sonicated target volume is achieved using bifocal wide holograms, about five times greater than that using a focused source, even when the conventional beam is in fact defocused because of aberrations.

The process of generating the hologram includes treatment planning, CT/MR image processing and both backward and forward simulation at the transducer central frequency on an Intel-Xeon workstation (E5-2680 at 2.8-GHz CPU, 256-GB RAM), taking a total of about 46 h. The physical lens is printed and ready in about 6 h, so the whole process of treating a specific patient lasts about 2 d from receipt of the CT image and segmented therapeutic target to manufacture of the holographic lens ready for the treatment. Shorter times should be possible by performing the simulations on high-performance computers, for example, using GPUs and/or faster industrial 3-D printers.

Acoustic holograms, however, have shown several drawbacks. On the one hand, when holograms are designed to generate a wide acoustic image, for example, bilaterally covering both nuclei, the gain is generally reduced. In fact, the lens is defocusing the therapeutic beam, and the acoustic energy is distributed in a higher area. A reduction of about 40% compared with the focused source was observed. This effect can be mitigated by increasing the amplitude of the source, but attention must be paid to additional effects outside the target, for example, heating effects in the skull. Selecting the temporal window to locate the source will help to mitigate skull heating as skull bones are thin in this region, which in fact is one of the main motivations of this work. The skull heating rate of this region has been estimated and compared with that of other targeted regions, the parietal and frontal bones. The total heating rate of the temporal bone window is approximately half that of the parietal bone and less than half that of the frontal bone. On the other hand, note that the acoustic images retrieved using holographic lenses are diffraction-limited versions of the target. When deep-brain nuclei are targeted using a limited-aperture source, such as the transducer used in this work, the generated acoustic image can spread in the axial direction. This effect increases the out-of-target region of wide holograms. The out-of-target volume can be mitigated by increasing the effective f -number of the source, that is, increasing

the aperture of the transducer. However, in the application proposed in this work, the temporal bone window limits the maximum aperture.

Note that the strategy selected to design the holograms in this work was a direct method, using virtual sources and time reversal; therefore, the lens was designed to produce a set of focal spots covering the target. Optimization techniques applied to transcranial propagation can help in designing holograms producing a better match between the diffraction-limited focal spots and the target (Li et al. 2021) or using multifrequency approaches (Brown et al. 2017). Other effects, such as the heating of the lens caused by acoustic absorption, can be mitigated using a water-coupling system or novel 3-D-printed materials with low absorption coefficients.

In a realistic scenario, the physical location of the acoustic hologram and the ultrasound source with respect to the patient's head will exhibit some degree of misalignment from the design location. The results of this work indicate that when using a focused transducer without a hologram, the shape and gain of the acoustic field produced hardly change when it is rotated around the center of the thalamus, which is logical because the incidence is always normal to the skull and the focused transducer presents a stable acoustic field. However, rotations with other references can result in uncontrolled focusing (Legon et al. 2018). On the other hand, when using acoustic holograms, the retrieved acoustic images are robust under relatively small misalignment. The degradation of the focal spots in terms of focal gain and targeting volumes was quantified. For the line hologram, the effect of misalignment is not as relevant as in the two-focus holograms because of the relative simplicity of the former compared with the latter. This can be seen by comparing the spreading of the focus for large rotations (or translations). For the line hologram, the volume outside the target at the maximum rotation error studied (17.5°) is increased 1.5 times compared with the original location, while for the two-line hologram is increased 4.5 times and for the two points it arrives at 30 times greater. This means that for this target, the transducer-lens system becomes less robust as the performed hologram increases in complexity. When the relative position between the head and the transducer is slightly different from the design, for example, a rotation of 5° or a translation of 4 mm, the acoustic images are still accurately reconstructed, even for translations larger than a wavelength, in all cases studied. The precision required can be achieved using image-guided systems (see, e.g., Pouliopoulos et al. 2020).

Because of the diffraction in the axial direction or the misallocation of the focus in the lateral dimensions, adjacent deep brain structures could be sonicated. If errors are made along the propagation axis of the

transducer (z -direction), structures such as the putamen and the globus pallidus could be partially sonicated. If the focus suffers translation in the negative x -axis (toward the parietal bone), the caudate nucleus can be affected, while if there is a shift in the positive x -axis and in both positive and negative z -axes, portions of the hippocampus and amygdala could be sonicated. All these structures except the amygdala participate in the coordination of fine motions and inhibit non-desired movements. Between other functions, the amygdala links such emotions as fear and aggression to human experiences. Finally, between both thalamic nuclei, we can find the third ventricle, which could potentially be sonicated. This structure is a part of the ventricles, connects both hemispheres and produces, contains and distributes cerebrospinal fluid. It is important to note that when translation and angle errors occur, we have observed that pressure gain decreases. Therefore, neuromodulatory or other bio-effects on out-of-target structures will be low or may not even occur. The higher peak pressure is observed only at the target and when the lens is at its design location.

CONCLUSIONS

In this work, acoustic holograms were numerically studied to target the thalamus through the temporal bone window using a 65-mm aperture transducer working at 650 kHz, and compared with a focused source with the same aperture and a curvature such that it can sonicate the center of both thalamic nuclei. The results indicate that holograms can enhance the targeting performance of the focused transducer in terms of treated volume and focal aberrations because they can improve focus quality and optimize sonicated volume ratio between brain and target tissues.

Secondary lobes and aberrations appearing with the use of single-element focused transducers can be corrected and focal spots can be adapted to the target even for bilateral sonications. These lenses also exhibit good focusing performance under relatively small mislocation of the therapeutic device. Nevertheless, when creating bilateral focusing, not only sonicated target volume increases, but out-of-target volume also increases, a consideration that must be taken into account when deciding what hologram best suits each therapeutical approach. Simple bilateral-point holograms minimize out-of-target focusing, while bifocal-plane holograms, even though while covering a larger area of the target deep-brain nuclei, may focus energy on adjacent central nervous system structures, which seems undesirable for neuromodulation applications (Legon et al. 2018), as a result of the limited angular spectrum of this transtemporal transducer. Enlarging the aperture of the transducer or using optimization methods to

generate the hologram has the potential to improve the targeting performance of broad holograms, and recent advances in spatial sound modulators can open new paths to design reconfigurable holograms and go beyond traditional phased-array systems (Ma *et al.* 2020).

The results obtained in this study also indicate that when a lens designed for one patient is used on a different person, the acoustic image cannot be reconstructed with accuracy because aberrations, even those produced at the temporal bone window, are strongly dependent on an individual's skull anatomy. The particular anatomy of the patient's head was found to be very relevant during transtemporal targeting, and patient-specific lenses should be designed to obtain accurate focusing, that is, to reconstruct diffraction-limited acoustic images without aberrations. Finally, targeting through the temporal window offers other practical advantages such as reduced skull heating and the need to shave only a small area of the head. These results pave the way for the design of accurate therapeutic devices for neuromodulation or drug delivery through blood–brain barrier opening in deep-brain structures using a low-cost and patient-specific approach.

Acknowledgments—This research has been supported by the Spanish Ministry of Science, Innovation and Universities (MICINN) through Grants IJC2018-037897-I, FPU19/00601 and PID2019-111436RB-C22 and by the Agència Valenciana de la Innovació through Grant INNCON/2021/8. Action was co-financed by the European Union through the Programa Operativo del Fondo Europeo de Desarrollo Regional (FEDER) of the Comunitat Valenciana 2014-2020 (ID-IFEDER/2018/022 and IDIFEDER/2021/004).

SUPPLEMENTARY MATERIALS

Supplementary material associated with this article can be found in the online version at doi:10.1016/j.ultrasmedbio.2022.01.010.

REFERENCES

- Aaslid R, Markwalder TM, Nornes H. Noninvasive transcranial Doppler ultrasound recording of flow velocity in basal cerebral arteries. *J Neurosurg* 1982;57:769–774.
- Adams C, Jones RM, Yang SD, Kan WM, Leung K, Zhou Y, Lee KU, Huang Y, Hynynen K. Implementation of a skull-conformal phased array for transcranial focused ultrasound therapy. *IEEE Trans Biomed Eng* 2021;68:3457–3468.
- Brown MD, Cox BT, Treeby BE. Design of multi-frequency acoustic kino-forms. *Appl Phys Lett* 2017;111 244101.
- Carstensen EL. Interaction of ultrasound with tissues. In: White D, Barnes R, (eds). *Ultrasound in medicine*. Boston: Springer; 1976. p. 517.
- Cobbold RS. *Foundations of biomedical ultrasound*. Oxford/New York: Oxford University Press; 2006.
- Coluccia D, Fandino J, Schwyzler L, O'Gorman R, Remonda L, Anon J, Martin E, Werner B. First noninvasive thermal ablation of a brain tumor with MR-guided focused ultrasound. *J Ther Ultrasound* 2014;2:17.
- Connor CW, Hynynen K. Patterns of thermal deposition in the skull during transcranial focused ultrasound surgery. *IEEE Trans Biomed Eng* 2004;51:1693–1706.
- Horodyckid C, Canney M, Vignot A, Boisgard R, Drier A, Huberfeld G, Francois C, Prigent A, Santin MD, Adam C, Willer JC, Lafon C, Chapelon JY, Carpentier A. Safe long-term repeated disruption of the blood–brain barrier using an implantable ultrasound device: A multiparametric study in a primate model. *J Neurosurg* 2017;126:1351–1361.
- Jiménez-Gambín S, Jiménez N, Benlloch JM, Camarena F. Holograms to focus arbitrary ultrasonic fields through the skull. *Phys Rev Applied* 2019;12 014016.
- Jiménez-Gambín S, Jiménez N, Benlloch JM, Camarena F, Pouliopoulos AN, Konofagou EE. Acoustic holograms for bilateral blood-brain barrier opening in a mouse model. *Transactions on Biomedical Engineering* 2021;. doi: 10.1109/TBME.2021.3115553 Accepted 27 September 2021.
- Jiménez-Gambín S, Jiménez N, Camarena F. Transcranial focusing of ultrasonic vortices by acoustic holograms. *Phys Rev Applied* 2020b;14 054070.
- Jones EG. *The thalamus*. New York: Springer Science & Business Media; 2012.
- Konofagou EE, Tunga YS, Choia J, Deffieux T, Baseria B, Vlachosa F. Ultrasound-induced blood–brain barrier opening. *Curr Pharm Biotechnol* 2012;13:1332–1345.
- Legon W, Ai L, Bansal P, Mueller JK. Neuromodulation with single-element transcranial focused ultrasound in human thalamus. *Hum Brain Mapping* 2018;39:1995–2006.
- Legon W, Adams S, Bansal P, Patel PD, Hobbs L, Ai L, Mueller JK, Meekins G, Gillick BT. A retrospective qualitative report of symptoms and safety from transcranial focused ultrasound for neuromodulation in humans. *Sci Rep* 2020;10:1–10.
- Li J, Lv Z, Hou Z, Pei Y. Comparison of balanced direct search and iterative angular spectrum approaches for designing acoustic holography structure. *Appl Acoust* 2021;175 107848.
- Lipsman N, Meng Y, Bethune AJ, Huang Y, Lam B, Masellis M, Herrmann N, Heyn C, Aubert I, Boutet A, Smith GS, Hynynen K, Black SE. Blood–brain barrier opening in Alzheimers disease using MR-guided focused ultrasound. *Nat Commun* 2018;9:1–8.
- Ma Z, Melde K, Athanassiadis AG, Schau M, Richter H, Qiu T, Fischer P. Spatial ultrasound modulation by digitally controlling microbubble arrays. *Nat Commun* 2020;11:1–7.
- Maimbourg G, Houdouin A, Deffieux T, Tanter M, Aubry JF. 3D-printed adaptive acoustic lens as a disruptive technology for transcranial ultrasound therapy using single-element transducers. *Phys Med Biol* 2018;63 025026.
- Maimbourg G, Houdouin A, Deffieux T, Tanter M, Aubry JF. Steering capabilities of an acoustic lens for transcranial therapy: Numerical and experimental studies. *IEEE Trans Biomed Eng* 2019;67:27–37.
- Mast TD. Empirical relationships between acoustic parameters in human soft tissues. *Acoust Res Lett Online* 2000;1:37–42.
- McDannold N, Arvanitis CD, Vykhodtseva N, Livingstone MS. Temporary disruption of the blood–brain barrier by use of ultrasound and microbubbles: Safety and efficacy evaluation in rhesus macaques. *Cancer Res* 2012;72:3652–3663.
- Melde K, Mark AG, Qiu T, Fischer P. Holograms for acoustics. *Nature* 2016;537:518–522.
- Monti MM, Schnakers C, Korb AS, Bystritsky A, Vespa PM. Non-invasive ultrasonic thalamic stimulation in disorders of consciousness after severe brain injury: A first-in-man report. *Brain Stimul* 2016;9:940–941.
- Pouliopoulos AN, Wu SY, Burgess MT, Karakatsani ME, Kamimura HA, Konofagou EE. A clinical system for non-invasive blood–brain barrier opening using a neuronavigation-guided single-element focused ultrasound transducer. *Ultrasound Med Biol* 2020;46:73–89.
- Qiu W, Bouakaz A, Konofagou EE, Zheng H. Ultrasound for the brain: A review of physical and engineering principles, and clinical applications. *IEEE Trans Ultrason Ferroelectr Freq Control* 2020;68:6–20.
- Robertson J, Martin E, Cox B, Treeby BE. Sensitivity of simulated transcranial ultrasound fields to acoustic medium property maps. *Phys Med Biol* 2017;62:2559.
- Schafer ME, Spivak NM, Korb AS, Bystritsky A. Design, development, and operation of a low-intensity focused ultrasound pulsation

- (LIFUP) system for clinical use. *IEEE Trans Ultrason Ferroelectr Freq Control* 2020;68:54–64.
- Schneider U, Pedroni E, Lomax A. The calibration of CT Hounsfield units for radiotherapy treatment planning. *Phys Med Biol* 1996;41:111.
- Sukovich JR, Cain CA, Pandey AS, Chaudhary N, Camelo-Piragua S, Allen SP, Hall TL, Snell J, Xu Z, Cannata JM, Teofilovic D, Bertolina JA, Kassell N, Xu Z. In vivo histotripsy brain treatment. *J Neurosurg* 2018;131:1331–1338.
- Sun J, Hynynen K. Focusing of therapeutic ultrasound through a human skull: A numerical study. *J Acoust Soc Am* 1998;104:1705–1715.
- Tillander M, Hokland S, Koskela J, Dam H, Andersen NP, Pedersen M, Tanderup K, Ylihautala M, Köhler M. High intensity focused ultrasound induced in vivo large volume hyperthermia under 3D MRI temperature control. *Med Phys* 2016;43:1539–1549.
- Treeby BE, Cox BT. k-Wave: MATLAB toolbox for the simulation and reconstruction of photoacoustic wave fields. *J Biomed Opt* 2010;15 021314.
- Wu SY, Aurup C, Sanchez CS, Grondin J, Zheng W, Kamimura H, Ferrera VP, Konofagou EE. Efficient blood–brain barrier opening in primates with neuronavigation-guided ultrasound and real-time acoustic mapping. *Sci Rep* 2018;8:1–11.
- Yushkevich PA, Piven J, Hazlett HC, Smith RG, Ho S, Gee JC, Gerig G. User-guided 3D active contour segmentation of anatomical structures: Significantly improved efficiency and reliability. *Neuroimage* 2006;31:1116–1128.